CrystEngComm

Accepted Manuscript

This article can be cited before page numbers have been issued, to do this please use: O.D. Chimitova, B.G. Bazarov, J. G. Bazarova, V. V. Atuchin, R. Azmi, A. Sarapulova, D. Mikhailova, G. Balachandran, A. Fiedler, U. Geckle, Yu. Prots, A. Komarek, T.A. Gavrilova, I. Prosvirin, Y. Yang, Z. Lin, M. Knapp and H. Ehrenberg, *CrystEngComm*, 2021, DOI: 10.1039/D1CE00118C.

ROYAL SOCIETY OF CHEMISTRY

rsc.li/crystengcomm

View Article Online
DOI: 10.1039/D1CE00118C

Corresponding authors:
O.D. Chimitova
Baikal Institute of Nature Management, Ulan-Ude 670047, Russia
Phone: +7 (3012) 433362
E-mail: chimitova_od@mail.ru

V.V. Atuchin
Institute of Semiconductor Physics, Novosibirsk 630090, Russia
Phone: +7 (383) 3308889
E-mail: atuchin@isp.nsc.ru

View Article Online
DOI: 10.1039/D1CE00118C

Crystal growth and properties of novel double magnetic molybdate $RbFe_5(MoO_4)_7$ with mixed Fe^{3+}/Fe^{2+} states and 1D negative thermal expansion

O.D. Chimitova[1], B.G. Bazarov[1], J.G. Bazarova[1], V.V. Atuchin[2,3], R. Azmi[4], A.E. Sarapulova[4], D. Mikhailova[4,5], G. Balachandran[4], A. Fiedler[4], U. Geckle[4], Yu. Prots[6], A. C. Komarek[6], T.A. Gavrilova[7], I.P. Prosvirin[8], Yi Yang[9], Zheshuai Lin[9], M. Knapp[4], H. Ehrenberg[4]

[1]Baikal Institute of Nature Management, Siberian Branch, Russian Academy of Sciences, Ulan-Ude 670047, Russia

[2]Laboratory of Optical Materials and Structures, Institute of Semiconductor Physics, SB RAS, Novosibirsk 630090, Russia

[3]Research and Development Department, Kemerovo State University, Kemerovo 650000, Russia

[4]Karlsruhe Institute of Technology (KIT), Institute for Applied Materials - Energy Storage Systems (IAM-ESS), Hermann-von-Helmholtz-Platz 1, D-76344 Eggenstein-Leopoldshafen, Germany

[5]IFW Dresden, Institute for Complex Materials, Helmholtzstrasse 20, 01069 Dresden, Germany

[6]Max Planck Institute for Chemical Physics of Solids, Nöthnitzer Str. 40, 01187 Dresden, Germany

[7]Laboratory of Nanodiagnostics and Nanolithography, Institute of Semiconductor Physics, SB RAS, Novosibirsk 630090, Russia

View Article Online
DOI: 10.1039/D1CE00118C

[8]Boreskov Institute of Catalysis, SB RAS, Novosibirsk 630090, Russia

[9]BCCRD, Key Laboratory of Functional Crystals and Laser Technology, Technical Institute of Physics and Chemistry, Chinese Academy of Sciences, Beijing 100190, China

Abstract

Single crystals of new composition $RbFe_5(MoO_4)_7$ were successfully grown by the flux method, and its crystal structure was determined using the X-ray single-crystal diffraction technique. The XRD analysis showed that the compound crystallizes in the monoclinic syngony, space group $P2_1/m$, with the unit cell parameters a = 6.8987(4), b = 21.2912(12) and c = 8.6833(5) Å, β = 102.1896(18)º, V = 1246.66(12) Å^3, Z (molecule number in the unit cell) = 2, R-factor (reliability factor) = 0.0166, T = 293(2) K. Raman spectra were collected on the single crystal to show the local symmetry of MoO_4 tetrahedra, after confirmation of crystal composition by the Energy Dispersive X-Ray Spectroscopy (EDS). The polycrystalline samples were synthesized by a solid-state reaction in the Ar atmosphere; the particle size and thermal stability were investigated by Scanning Electron Microscopy (SEM) and Differential Scanning Calorimetry (DSC) analyses. The compound decomposes above 1073 K in the Ar atmosphere with the formation of a Fe(III) molybdate. The thermal expansion coefficient along c direction has the value α = – 1.3 ppm/K over the temperature range of 298-473 K. Magnetic measurements revealed two maxima in the magnetization below 20 K, and the paramagnetic behavior above 50 K with the calculated paramagnetic moment of 12.7 μB per formula unit is in good agreement with the presence of $3Fe^{3+}$ and $2Fe^{2+}$ in the high-spin (HS) state. The electronic structure of $RbFe_5(MoO_4)_7$ is comparatively evaluated by X-ray photoelectron spectroscopy (XPS) and Density functional theory (DFT) calculations.

Keywords: molybdate; crystal structure; ferromagnetic property; Raman spectroscopy; electronic structure

View Article Online
DOI: 10.1039/D1CE00118C

1. Introduction

Magnetic and multiferroic materials represent an important part of modern technologies, which offer a wide range of new applications. Due to the relation of the magnetic properties to an external electric field and, conversely, by setting the dielectric properties as a function of the magnetic field, numerous multifunctional materials can be obtained. As an example of applications [1-3], it can be provided multiple state memory elements, in which data are stored both in the electric and magnetic polarizations, and novel memory media. Fe-containing materials can exhibit simultaneously ferrimagnetism and ferroelectricity with magnetic and electrical Curie transitions [4-7]. Thus, many investigations of crystal and electronic structures have already been carried out with the complex Fe-containing compositions, and the materials are of great interest with scientists [8-14]. On the other hand, it is well known that high-quality molybdate crystals can be prepared at comparatively low temperatures [15-20], and this feature is extremely significant for industrial production. Thus, the development of new Fe-containing compounds in the chemical class of molybdates with promising physical properties is highly topical.

In the system Rb_2MoO_4–$Fe_2(MoO_4)_3$, the molybdates $RbFe(MoO_4)_2$ and $Rb_5Fe(MoO_4)_4$ have been known for a long time [21-23]. The composition, symmetry and unit cell parameters of $RbFe(MoO_4)_2$ indicates that it belongs to the structural type of glaserite-like $KAl(MoO_4)_2$ [24, 25]. Below the Néel temperature of T_N = 3.8 K, trigonal $RbFe(MoO_4)_2$ is a quasi-two-dimensional antiferromagnet on a triangular lattice. At the temperature 190 K, the crystal exhibits the phase transition from the structure *P*-3*m*1 stable at room temperature to that of the *P*-3 symmetry [26]. This molybdate belongs to the family of magnetic solids with the general composition $AM(XO_4)_2$, where A is an alkali metal, M = Cr^{3+}, Mn^{3+} or Fe^{3+}, and X = Mo, W, S or Se [27, 28]. This group of

View Article Online
DOI: 10.1039/D1CE00118C

compounds is characterized by the polymorphism of layered trigonal structures and triangular-lattice magnetic phases [29-32]. Besides, $RbFe(MoO_4)_2$ possesses multiferroic properties, as it was described in the recent work [33]. The other molybdate $Rb_5Fe(MoO_4)_4$ can crystallize in two different modifications and the low-temperature β-$Rb_5Fe(MoO_4)_4$ undergoes a phase transition at 693K to high-temperature phase α-$Rb_5Fe(MoO_4)_4$ [23, 34]. Recently, the monoclinic double polymolybdate $Rb_3FeMo_4O_{15}$ has been described and available information on the binary system Rb_2MoO_4–$Fe_2(MoO_4)_3$ was summarized in [35]. It should be mentioned that, in all known Rb-Fe molybdates, iron ions are in the formal valence state Fe^{3+}. It will be interesting to investigate also the compositions with the mixed oxidation state of Fe and the physical properties of the obtained molybdates. Besides, the changing of monovalent cation can influence the magnetic structure of double molybdate.

In the previous work [36],, during the investigation of molybdate system Cs–$Fe^{II,III}$–Mo–O, new compounds, $CsFe_5(MoO_4)_7$, $Cs_2Fe_2(MoO_4)_3$ and $Cs_4Fe(MoO_4)_3$, were found and the structural characteristics of the molybdates were evaluated. Among those, molybdate $CsFe_5(MoO_4)_7$ represented a new structural type. It contains Fe^{3+} and Fe^{2+} ions and orders magnetically below T_C = 10 K. A canted antiferromagnetic structure was proposed. Then, it could be reasonably assumed that the molybdate system Rb–$Fe^{II,III}$–Mo–O, besides earlier known rubidium molybdates, also includes the first time obtained $RbFe_5(MoO_4)_7$ composition isostructural to $CsFe_5(MoO_4)_7$. Thus, the main objective of the present study is the preparation of $RbFe_5(MoO_4)_7$ crystals and exploration of their crystal and electronic structure, as well as magnetic properties.

2. Experimental

The initial reactants used for the synthesis were $RbNO_3$, Fe_2O_3, FeO, MoO_3 (all Alfa Aesar) with the purity degree >99.99 % (metal basis). The first step was the Rb_2MoO_4 synthesis by the solid-state reaction between rubidium nitrate and molybdenum oxide at the stepwise annealing up to 923

View Article Online
DOI: 10.1039/D1CE00118C

K. A detailed description of this solid-state synthesis can be found elsewhere [37, 38]. From the technological point of view, the preparation of $RbFe_5(MoO_4)_7$ is not trivial because of an easy oxidation of Fe^{2+} to Fe^{3+}, and the process of preparation should be conducted in the inert atmosphere. The $RbFe_5(MoO_4)_7$ single crystals were grown by the flux method from the stoichiometric mixture of Rb_2MoO_4, Fe_2O_3, FeO and MoO_3 according to the following reaction:

$$Rb_2MoO_4 + 4FeO + 3Fe_2O_3 + 13MoO_3 \rightarrow 2RbFe_5(MoO_4)_7 \quad (1)$$

The mixture was put into a silica tube which was evacuated and sealed under vacuum (10^{-4} mbar). The tube was heated up to 1073 K, held at this temperature for 2 h and then cooled at 5 K/h down to room temperature. The cooled reaction tube was broken and the ingot was removed. The red-brown single crystals were carefully selected from the ingot using an optical microscope. The polycrystalline sample was prepared in the oven inside the Ar filled glove box at the temperature 893K for 24h according to equation (1).

The high quality single crystal of $RbFe_5(MoO_4)_7$ was selected and mounted onto glass capillaries for the X-ray structure analysis. The diffraction data were collected at room temperature with a Bruker D8 VENTURE X-ray diffractometer (Bruker AXS, Karlsruhe, Germany) with the Mo-$K\alpha_1$ radiation using a bent graphite monochromator. The reflection intensities were integrated with the SAINT subprogram in the Bruker Suite software package, and a multi-scan absorption correction was applied using SADABS [39]. The structure was solved by direct methods [40] and refined by full-matrix least-squares on F^2 using the SHELX97 program set [41]. The polycrystalline samples were characterized by X-ray powder diffraction using a STOE STADI P diffractometer (Co−$K_{\alpha1}$ radiation). The structural parameters of $RbFe_5(MoO_4)_7$ were determined by Rietveld refinement using the program FullProf within the software package WinPLOTR [42].

The Raman spectra were collected using the Raman microscope Horiba Scientific Lab RAM HR Evolution (Plan Fluorit) on the grown single crystals. The chemical composition of selected crystals

View Article Online
DOI: 10.1039/D1CE00118C

was confirmed by the SEM-EDS analysis (Zeiss GmbH FE-SEM MERLIN Oberkochen and Bruker, SDD, XFlash 6/60, Berlin, Germany).

The thermogravimetric, Differential Thermal Analysis and Differential Scanning Calorimetry (TG-DTA/DSC) were carried out under the Ar atmosphere (Netzsch Jupiter 449 C). The thermal behavior of polycrystalline $RbFe_5(MoO_4)_7$ was also investigated *in situ* with high temperature synchrotron radiation diffraction measurements of polycrystalline materials in the sealed capillaries using the European Synchrotron Radiation Facility (ESRF, Grenoble, France) and a German Electron Synchrotron (DESY, Hamburg, Germany). The wavelengths were λ = 0.40073 Å and λ = 0.20719 Å, respectively.

The polycrystalline samples morphology was studied by scanning electron microscopy (SEM) using an LEO 1430 device. The $RbFe_5(MoO_4)_7$ magnetization measurements were performed with a superconducting quantum interference device (SQUID) from Quantum Design, using powder polycrystalline material. The measurements were carried out in field-cooled (FC) and zero-field cooled (ZFC) modes in the temperature range of 1.8-370 K with the external magnetic field of 0.05 T. The field dependence of magnetization was measured up to 5 T at 2 and 13 K. Magnetic susceptibility in the paramagnetic region was analyzed in terms of the modified Curie-Weiss law with a temperature-independent paramagnetic contribution χ_0: $\chi = C/(T-\theta) + \chi_0$, where the Curie constant $C = N_A\mu_{eff}^2/3k_B$ yields the paramagnetic effective moment μ_{eff}.

The X-ray photoelectron spectroscopy measurements were made using a K-Alpha™ instrument (Thermo Fisher Scientific, East Grinstead, UK) applying a microfocused, monochromated Al Kα X-ray source with a 400 μm spot size. The K-Alpha™ charge compensation system was applied during the analysis, using electrons with the energy of 8 eV and low energy argon ions to prevent any localized charge build-up. The data acquisition and processing using the Thermo Avantage software are described in Parry et al. [43] To fit the obtained spectra, one or more Voigt profiles with a binding energy uncertainty of ±0.2 eV are used. For quantification, the analyzer transmission

View Article Online
DOI: 10.1039/D1CE00118C

function, Scofield sensitivity factors [44] and effective attenuation lengths (EALs) for photoelectrons are applied. EALs are calculated using the standard TPP-2M formalism [45]. The collected spectra are referenced to the C 1s peak of hydro-carbons at the binding energy of 285.0 eV which is controlled by means of the well-known photoelectron peaks of metallic Cu, Ag, and Au.

3. Computation methods

The spin-polarized first-principles band structure calculations for $RbFe_5(MoO_4)_7$ were performed by CASTEP [46, 47], a plane-wave pseudopotential total energy package based on the density functional theory (DFT) [48]. The functionals developed by Ceperley, Alder, Perdew, and Zunger (CA-PZ) in the form of local density approximation (LDA) [49, 50] were adopted to describe the exchange-correlation energy. The optimized norm-conserving pseudopotentials [51] in the Kleinman-Bylander [52] form for all the elements were used to model the effective interaction between atom cores and valence electrons, allowing the adoption of a relatively small basis set without compromising the computational accuracy. The Rb $4s^24p^65s^1$, Fe $3d^64s^2$, Mo $4d^55s^1$ and O $2s^22p^4$ electrons were treated as valence electrons, and a high kinetic energy cutoff of 800 eV was chosen. Moreover, in order to describe the localized d-orbitals in iron atoms, the LDA + U method [53, 54] was adopted by setting the on-site orbital dependent Hubbard U energy as $U_d = 6$ eV.

4. Result and Discussion

Crystal structure determination

The crystal structure of $RbFe_5(MoO_4)_7$ was solved using single crystal X-ray diffraction and refined in the space group $P2_1/m$ (Table 1). The compound is isostructural with $CsFe_5(MoO_4)_7$. The structure consists of separate FeO_6-octahedra with the average Fe(1)–O distance of 2.015(2)Å and zigzag Fe_4O_{18}-units of edge-sharing FeO_6-octahedra with the average Fe(2)–O and Fe(3)-O distances of 2.018(6)Å and 2.071 Å respectively which are connected *via* corners with MoO_4-

View Article Online
DOI: 10.1039/D1CE00118C

tetrahedra (average Mo–O distance - 1.76(4) Å) (Figure 1). There is no direct contact between MoO_4 units. The comparative analysis of interatomic distances in $CsFe_5(MoO_4)_7$ and $RbFe_5(MoO_4)_7$ revealed the decrease in most of Fe-O bond lengths during the Cs substitution by Rb atoms. The atomic coordinates and equivalent isotropic thermal displacement parameters are listed in Tables 1S-3S (Supporting information). In the $RbFe_5(MoO_4)_7$ structure, rubidium atoms occupy the channels along the *a*-axis (Figure 1). From the structural considerations in the a-direction at elevated temperatures, the high ionic conductivity of Rb ions can be proposed. The supplementary data CCDC 1992524 contain the crystallographic data determined for the $RbFe_5(MoO_4)_7$ compound. These data can be obtained free of charge via http://www.ccdc.cam.ac.uk/conts/retrieving.html, or from the Cambridge Crystallographic Data Centre (12 Union Road, Cambridge CB2 1EZ, UK; fax: (+44)1223-336-033; or e-mail: deposit@ccdc.cam.ac.uk.)

The chemical composition of grown single crystals was tested by the EDS methods. The representative EDS spectrum is shown in Figure 1S (Supporting information). As seen in Figure 1S, the chemical element ratio in the selected crystals determined by the EDS analysis is in a good agreement with the nominal composition.

Single crystals of $RbFe_5(MoO_4)_7$ were also used for the recording of Raman spectra. The parallel measurements, repeated on three different crystals, provided approximately the same spectra (Figure 2). The description of the modes was related to the nomenclature, which is commonly used for complex molybdates [10, 32, 55, 56]. In the monoclinic $RbFe_5(MoO_4)_7$ structure, Mo^{6+} ions occupy the 4f and 2e sites of the C_s symmetry. The T_d point symmetry of MoO_4^{2-} tetrahedrons is reduced in the unit cell to C_s and each next vibrational mode splits due to the interactions of two molecules in the primitive cell. In the spectra of $RbFe_5(MoO_4)_7$ sample, 9 Raman-active bands are expected (Table 2). However, the number of experimentally observed bands is less, for example, for the asymmetric bending mode. The absence of the remaining predicted modes can be attributed to

View Article Online
DOI: 10.1039/D1CE00118C

the accidental degeneracy and/or low intensity of the corresponding bands. Besides, the coupling of the librational and bending modes of MoO_4 units should be taken into account in the factor group approach because, usually, the librational motions are frozen and strongly mixed with internal modes. Four internal modes of free molybdate unit [T_d symmetry: $\nu_1(A_1)$, $\nu_2(E)$, $\nu_3(F_2)$ and $\nu_4(F_2)$] are transformed for the C_{2h} symmetry into: symmetric and asymmetric stretching modes of the MoO_4 groups [$\nu_s(MoO_4)$: A_g+B_u and ν_{as} (MoO_4): $2(A_g+B_u)$ + (A_u+B_g)] and symmetric and asymmetric bending modes [δ_s (MoO_4): (A_g+B_u) + (A_u+B_g) and δ_{as} (MoO_4): $2(A_g+B_u)$ + (A_u+B_g)]. The splitting of A_g Raman mode can be explained by defects in the crystal structure of the selected single crystal, like stacking and cracks, which make the structure different from an ideal monoclinic $P2_1/m$ structure. In comparison with the previously published data about the vibrational spectra of molybdates [57], our Raman spectra obtained on single crystals are in a closer agreement with the result of factor group analysis.

Characterization of powdered samples

To investigate the physical properties, the polycrystalline $RbFe_5(MoO_4)_7$ sample was prepared by the solid-state reaction (1) in a dry Ar atmosphere. The stoichiometric mixture of Rb_2MoO_4, FeO, Fe_2O_3 and MoO_3 was used as a raw material. The synthesis was carried out at 893K for 24 h. The synthesized product is represented as a dark brown powder. The monoclinic structure solved on the single crystal was applied as a starting model for Rietveld refinement of the structural parameters of the polycrystalline material. The XRD pattern recorded from the powder sample is shown in Figure 3. All peaks are successfully attributed to $RbFe_5(MoO_4)_7$ and this verifies a good phase purity of the powder sample. The structural parameters (a = 6.8949(1) Å, b = 21.2844(2) Å, c = 8.6742(1) Å, β = 102.1781(5), Co Kα-radiation, Bragg R-factor = 10.3, Rf-factor = 7.8, Chi2 = 1.89) obtained by Rietveld refinement were in excellent agreement with those determined by the single crystal structure analysis (Table 1). It is confirmed that the polycrystalline compound with the unit cell

View Article Online
DOI: 10.1039/D1CE00118C

parameters for the monoclinic structure $P2_1/m$ have been obtained. The structure parameters have lower values than for the isostructural $CsFe_5(MoO_4)_7$ [36] compound because of differences in the monovalent element's radii ($R_{ion}(Cs)>R_{ion}(Rb)$).

The particle morphology is shown in Figure 4. As seen, the $RbFe_5(MoO_4)_7$ particles are partly agglomerated, and it is a typical feature for powder molybdate products [37, 38, 55]. The formation of well faceted grains with dimensions 1-3 μm is evident in Figure 4 (b) and it verifies the optimal selection of the temperature/time synthesis conditions.

In contrast to $CsFe_5(MoO_4)_7$ [36], the temperature dependences of magnetization (Figure 5) of $RbFe_5(MoO_4)_7$ do not show a difference between zero-field cooled (ZFC) and field cooled (FC) measurements below 20 K that can indicate the absence of any ferro- or ferrimagnetic ordering in $RbFe_5(MoO_4)_7$. Instead, we observed two maxima in the magnetization at T_1 = 12 K, and T_2 = 17 K. At temperatures above 50 K, the magnetization obeys the modified Curie-Weiss law $\chi = C/(T-\theta) + \chi_0$ with θ = -13.6(1) K and χ_0 = -1.8(2)*10^{-3} emu/mol*G. The negative Curie-Weiss temperature of -13.6(1) K indicates dominant antiferromagnetic interactions in the compound. The paramagnetic moment of μ_B =12.7(1) μB/f.u. of Fe-ions was calculated from the Curie-constant C as an average value from FC and ZFC data. For comparison, a theoretical paramagnetic moment was calculated assuming the existence of 3HS-Fe^{3+} and 2HS-Fe^{2+} in the formula unit: μ_{teor} = 12.4 μB/f.u. A very good agreement between experimental and calculated values confirms the proposed oxidation states of Fe in the compound. The field dependence of the magnetization between 2 and 25 K (Figure 5) does not show any intermediate steps that may point that the magnetic structure of $RbFe_5(MoO_4)_7$ is not as complex as for the Cs analogue, which shows a stepwise increase of the magnetization with the field at 2K [36]. However, low-temperature neutron powder diffraction experiments are necessary to confirm this suggestion. For $CsFe_5(MoO_4)_7$, the antiferromagnetic structure at 0 T was described by the combination of two propagation vectors **k** = (1/2, 0, 0) and **k** = (0, 0, 0) with the magnetic moments of 2.6, 1.6 and 3.5 μB for three independent Fe sites [36].

View Article Online
DOI: 10.1039/D1CE00118C

The XRD patterns, recorded at different temperatures up to 1173 K, are shown in Figure 2S. As one can see, the $RbFe_5(MoO_4)_7$ structure is persistent up to 1073 K and, at higher temperatures, the decomposition appears. The analysis of the XRD pattern recorded at 1173 K indicates the presence of $Fe_2(MoO_4)_3$ (ICSD 80449), $Rb_2Mo_3O_{10}$ (ICSD 48213) and $Rb_2Mo_2O_7$ (ICSD 249126), and some amorphous components. The phase instability above 1073 K was confirmed by the thermal analysis, and the results are shown in Figure 6. After heating till 1073 K in the Ar atmosphere, the sample is irreversibly decomposed. Note, that there is no detectable mass change up to 1173 K and, therefore, a noticeable evaporation of MoO_3 during the heating should be excluded. The thermal effects observed at 1093 K and 783 K could be attributed to the solidification point of decomposition products and the phase transition of $Fe_2(MoO_4)_3$ [58], respectively.

The temperature dependences of the cell parameters and cell volume are presented in Figure 7. The thermal expansion coefficient (TEC) is a key thermal property in the development of high temperature materials. On the temperature dependence of the c parameter, two regions with negative and positive thermal expansions can be observed. As calculated from the linear part of the low temperature dependence region 298-473 K of parameter *c*, the TEC has the value $\alpha = -1.3$ ppm/K, and, at the same time, high temperature region 473-1073 K has the value $\alpha = 2.1$ ppm/K. Parameter b has, accordingly, the value $\alpha = 8.7$ ppm/K of the TEC for the region 298-473 K and $\alpha = 10$ ppm/K - for the region 473-1073 K (ppm = 10^{-6}). In comparison with the industrial materials Mo (5.7 ppm/K) and W(4.8 ppm/K) for the same temperature region (293-1073 K), the positive TEC for the parameter a has values $\alpha = 11$ ppm/K in the region 298-473 K and $\alpha = 6.8$ ppm/K in the high temperature region 473-1073 K. The volumetric thermal expansion coefficient is observed to be 18.4 ppm/K below 473 K and 19.2 ppm/K - at the temperature higher than 473 K. In general, the structure keeps the monoclinic space group $P2_1/m$ in the whole studied temperature range up to the decomposition temperature. The extremum on the temperature dependence of the *c* parameter can be explained by the phase transition with very close crystal structures of low-temperature and high-

View Article Online
DOI: 10.1039/D1CE00118C

temperature phases and it was observed for the molybdate system before [59]. In this kind of transition for the low symmetry space group, the oxygen atoms can be reoriented, but still related by the same symmetry operations.

In the XPS data, the Mo 3d core level spectrum deconvolution reveals two spin–orbit doublets, belonging to the Mo $3d_{5/2}$ and Mo $3d_{3/2}$ core levels at the binding energies of 232.8 and 236.0 eV originating from molybdenum ions in the oxidation state +6 (Figure 8(a)) [60, 61]. The second spin–orbit doublet with the maxima at 238.1 and 246.6 eV can be attributed to the Rb $3p_{3/2}$ and Rb $3p_{1/2}$ core levels of rubidium ions. The Rb 3d core level spectrum can be fitted by one spin–orbit doublet (Figure 8(b)) with the maxima at the binding energies of 109.9 and 111.4 eV attributed to the Rb $3d_{5/2}$ and Rb $3d_{3/2}$ core levels of rubidium ions in the oxidation state +1 [62-68]. In particular, the Fe $2p_{3/2}$ XP spectrum show two maxima at 709.2 and 711.6 eV as a hint of the mixed oxidation state for iron ions. The Fe $2p_{3/2}$ XP spectrum were deconvoluted following the approach of A. P. Grosvenor et al [69] for the interpretation of complex Fe spectra. Therefore, the Fe $2p_{3/2}$ spectrum could be successfully fitted with the set of Fe^{2+} (orange color) and Fe^{3+} (purple color) 2p multiplets, as shown in Fig. 8(c), keeping the FWHM, spacing and intensity ratio of the spectral multiplet peaks consistent with those of iron oxides investigated in the literature [69, 70]. As a result, 40% of the total Fe content could be attributed to Fe^{2+} ions and the rest 60% of it - to Fe^{3+} ions, and it is in a very good agreement with the charge neutrality calculations expected from the chemical formula of the material. Finally, the C 1s core level spectrum deconvolution gives three components at the binding energies of 285.0, 286.4 and 288.9 eV, belonging to C–C/C–H, C–O and C=O species, respectively (Figure 8(e)) and deconvoluting the O 1s core level spectrum reveals components at the binding energies of 530.9 and 532.4 eV, and it can be attributed to Metal-Oxygen bonds and carboxylic surface groups, respectively (Figure 8(d)) [71].

View Article Online
DOI: 10.1039/D1CE00118C

The calculated density of states (DOS) and the partial densities of states (PDOS) projected on the constitutional atoms in $RbFe_5(MoO_4)_7$ are shown in Figure 9. In the electronic structure, only the outer-shell valence electrons are exhibited because the first-principles calculation takes into account only these electrons. One may easily find that the DOS and PDOS are in a reasonable agreement with the measured XPS spectrum when the whole experimental XPS spectrum is moved to a lower binding energy of 3.5 eV. The red-shift of the XPS spectrum is because the Fermi level has different selection criteria in the experiment and calculation. The PDOS reveals that the Fe 3d orbitals have an obvious split at different spin states: the spin-up electrons mostly occupy the valence bands between −15 to −5 eV, while the spin-down electronic states are mostly located at the bottom of conduction bands. No spin-split is observed for other atoms. This implies that $RbFe_5(MoO_4)_7$ might possess the strong magnetism which resulted from the iron atoms. In addition, several electronic characteristics are displayed in the PDOS: (i) the electronic states lower than −15 eV are mainly composed of the isolated inner-shell states with Rb 4s, Mo 4d and O 2s orbitals which have little interaction with other orbitals. (ii) The upper part of valence bands consists mainly of the orbitals of Mo (4d), O (2p) and Fe (3d) and a quite strong hybridization is present among the Mo-O and the Fe-O atoms.

5. Conclusions

Newly discovered $RbFe_5(MoO_4)_7$ crystallizes in the monoclinic symmetry ($P2_1/m$, a = 6.8987(4) Å, b = 21.291(1) Å, c = 8.6833(5) Å, β = 102.190(2)°, Z = 2) and is isostructural to $CsFe_5(MoO_4)_7$, which represents its structure type. A three-dimensional framework of this structure contains three crystallographically independent Fe-sites and consists of isolated FeO_6-octahedra and Fe_4O_{18}-units of edge-sharing FeO_6-octahedra, which are connected with MoO_4-tetrahedra via corners. The obtained compound irreversibly decomposes in the inert atmosphere at 1073 K according to the

View Article Online
DOI: 10.1039/D1CE00118C

DSC-TG results, has a good crystallinity in the SEM pictures and a low thermal expansion coefficient for the unit cell parameters.

On the example of $RbFe_5(MoO_4)_7$, it is shown that Cs^+ ion in $CsFe_5(MoO_4)_7$ basic structure can be substituted by other alkali cations. The exchange of cations plays an essential role in the variation of magnetic properties. The magnetic structure becomes simpler with smaller Rb^+ ions and shows no difference between zero-field cooled (ZFC) and field cooled (FC) measurements below 20 K. The material $RbFe_5(MoO_4)_7$ has dominant antiferromagnetic interactions above 50 K. An excellent agreement between experimental (μ_B =12.7(1) μB/f.u.) and calculated (μ_{teor} =12.4 μB/f.u.) values of iron paramagnetic moment confirms the proposed oxidation states of Fe in the compound. The mixed oxidation state +2.6 for iron ions was also confirmed with XPS data, where 40% of the total Fe content could be attributed to Fe^{2+} ions and the rest 60% of it - to Fe^{3+} ions, and it is in very good agreement with the charge neutrality calculations expected from the chemical formula of the material. For a detailed description of the magnetic structure, further low-temperature neutron and synchrotron radiation powder diffraction measurements are required.

Acknowledgements

This work was partly supported by the DAAD (A-13-00078), the state order of BINM SB RAS (project No. 0339-2016-0007) and RFBR Grant 18-03-00557. The authors are very grateful to Dr. Alexander Tsirlin (University of Augsburg, Germany) for the help in thermal expansion measurements at the European Synchrotron Radiation Facility (ESRF), Grenoble, France. We acknowledge DESY (Hamburg, Germany), a member of the Helmholtz Association HGF, for the provision of experimental facilities. Parts of this research were carried out at PETRA III and we would like to thank Dr. Martin Etter for assistance in using P02.1. The ZEISS MERLIN SEM was financially supported by the Federal Ministry of Economics and Technology on the basis of a decision by the German Bundestag within the BMBF grant no. 03ET6017.

View Article Online
DOI: 10.1039/D1CE00118C

Author Contributions: Conceptualization: O.D. Chimitova, D. Mikhailova, B.G. Bazarov, J.G. Bazarova; investigation: O.D. Chimitova, A.E. Sarapulova; data curation, methodology: T.A. Gavrilova, I.P. Prosvirin, A. Fiedler, U. Geckle, Yi Yang, Zheshuai Lin; writing—original draft preparation: A.E. Sarapulova, D. Mikhailova; writing—review and editing: V.V. Atuchin, O.D Chimitova D. Mikhailova; thermal analysis: G. Balachandran; XPS analysis: R. Azmi; SEM: V.V. Atuchin; X-ray structure analysis: Yu. Prots, A. C. Komarek; Project administration: M. Knapp, H. Ehrenberg; All authors have read and agreed to the published version of the manuscript.

References

1. M. E. Lines, A. M. Glass, Principles and applications of ferroelectrics and related materials. OUP oxford, 2001. 680 p.
2. S. W. Cheang, R. Ramtsh, Multiferroics: Past, presents and future, Phys. Today 63 (2010) 38-43.
3. T. Lottermose, T. Lonkai, U. Amann, D. Hohlwein, J. Ihringer, M. Fiebig, Magnetic phase control by an electric field, Nature 430 (6999) (2004) 541-544.
4. S. G. Greculeasa, P. Palade, G. Schinteie, A. Leca, F. Dumitrache, I. Lungu, G. Prodan, A. Kuncser & V. Kuncser Tuning structural and magnetic properties of Fe oxide nanoparticles by specific hydrogenation treatments. Scientific Reports 10 (2020)17174.
5. N. Ikeda, H. Ohsumi, K. Ohwada, K. Ishii, T. Inami, K. Kakurai, Y. Murakami, K. Yoshii, S. Mori, Y. Horibe, H. Kito. Ferroelectricity from iron valence ordering in the charge-frustrated system $LuFe_2O_4$, Nature 438 (7054) (2005) 1136-1138.
6. K. Balamurugan, N. Harish Kumar, P. N. Santhosh. Multiferroic properties of $Bi_{1/2}Sr_{1/2}FeO_3$. Journal of Applied Physics, 105 (7) (2009) 07D909.
7. D.A. Vinnik, D.A. Zherebtsov, L.S. Mashkovtseva, S. Nemrava, M. Bischoff, N.S. Perov, A.S. Semisalova, I.V. Krivtsov, L.I. Isaenko, G.G. Mikhailov, R. Niewa, Growth, structural and

magnetic characterization of Al-substituted barium hexaferrite single crystals, J. Alloys Compd. 615 (2014) 1043-1046.

View Article Online
DOI: 10.1039/D1CE00118C

8. A.P. Grosvenor, B.A. Kobe, M.C. Beisinger, N.S. McIntyre, Investigation of multiplet splitting of Fe 2p XPS spectra and bonding in iron compounds, Surf. Interface Anal. 36 (12) (1984) 1564-1574.
9. Xiandong Wang, Kevin R. Heier, Charlotte I. Stern, Kenneth R. Poeppelmeier, Crystal structure and Raman spectroscopy of $FeVMoO_7$ and $CrVMoO_7$ with Mo=O double bonds, Inorg. Chem. 37 (1998) 3252-3256.
10. M. Mączka, A. Pietraszko, A.G. Souza Filho, P.T.C. Freire, J. Mendes Filho, J. Hanuza, Structural and vibrational properties of $K_3Fe(MoO_4)_2(Mo_2O_7)$ – a novel layered molybdate, J. Phys.: Condens. Matter 21 (2009) 095402.
11. R.L. Frost, S. Bahfenne, J. Čejka, J. Sejkora, J. Plášil, S.J. Palmer, E.C. Keefe, I. Němec, Dussertite $BaFe^{3+}{}_3(AsO_4)_2(OH)_5$ – a Raman spectroscopic study of a hydroxy-arsenate mineral, J. Raman Spectr. 42 (2011) 56-61.
12. V.V. Atuchin, D.A. Vinnik, T.A. Gavrilova, S.A. Gudkova, L.I. Isaenko, Xingxing Jiang, L.D. Pokrovsky, I.P. Prosvirin, L.S. Mashkovtseva, Zheshuai Lin, Flux crystal growth and electronic structure of $BaFe_{12}O_{19}$ hexaferrite, J. Phys. Chem. C 120 (2016) 5114-5123.
13. O.P. Taran, A.B. Ayusheev, O.I. Ogorodnikova, I.P. Prosvirin, L.A. Isupova, V.N. Parmon, Perovskite-like catalysts $LaBO_3$ (B = Cu, Fe, Mn, Co, Ni) for wet peroxide oxidation of phenol, Appl. Cat. B: Ebvironment 180 (2016) 86-93.
14. A.H. Reshak, Spin polarization in filled skutterudites $LaFe_4Pn_{12}$ (Pn = P, As and Sb), J. Magn. Magn. Mater. 401 (2016) 684-694.
15. V.V. Atuchin, T.A. Gavrilova, T.I. Grigorieva, N.V. Kuratieva, K.A. Okotrub, N.V. Pervukhina, N.V. Surovtsev, Sublimation growth and vibrational microspectrometry of α-MoO_3 single crystals, J. Cryst. Growth 318 (2011) 987-990.

16. Pinglu Shi, Zhiguo Xia, M.S. Molokeev, V.V. Atuchin, Crystal chemistry and luminescence properties of red-emitting $CsGd_{1-x}Eu_x(MoO_4)_2$ solid-solution phosphors, Dalton Trans. 43 (2014) 9669-9676.

17. V.V. Atuchin, N.V. Ivannikova, A.I. Komonov, N.V. Kuratieva, I.D. Loshkarev, N.V. Pervukhina, L.D. Pokrovsky, V.N. Shlegel, The low thermal gradient Czochralski crystal growth and microstructural properties of a Pb_2MoO_5(20-1) cleaved surface, CrystEngComm 17 (2015) 4512-4516.

18. Chang Sung Lim, A. Aleksandrovsky, M. Molokeev, A. Oreshonkov, V. Atuchin, The modulated structure and frequency upconversion properties of $CaLa_2(MoO_4)_4:Ho^{3+}/Yb^{3+}$ phosphors prepared by microwave synthesis, Phys. Chem. Chem. Phys. 17 (2015) 19278-19287.

19. N. Joseph, J. Varghese, T. Siponkoski, M. Teirikangas, M.T. Sebastian, H. Jantunen, Glass-free $CuMoO_4$ ceramic with excellent dielectric and thermal properties for ultralow temperature cofired ceramic applications, ACS Sustainable Chem. Eng. 4 (10) (2016) 5632-5639.

20. Chang Sung Lim, A.S. Aleksandrovsky, M.S. Molokeev, A.S. Oreshonkov, V.V. Atuchin, Triple molybdate scheelite-type upconversion phosphor $NaCaLa(MoO_4)_3:Er^{3+/}Yb^{3+}$: structural and spectroscopic properties, Dalton Trans. 45 (2016) 15541-15551.

21. V. K. Trunov and V. A. Efremov, About double alkali- and trivalent elements, Zh. Neorg. Khim. 16 (7) (1971) 2026-2027.

22. Yu. A. Velikodnyi, Extended Abstract of Candidate's Dissertation in Chemistry (Moscow, 1975).

23. B. I. Lazoryak and V. A. Efremov, About double molybdates $Me_5TR(MoO_4)_4$, Kristallografiya 32 (2) (1987) 378- 384.

24. R. F. Klevtsova and P. V. Klevtsov, Synthesis and crystal structure of double molybdates $KR(MoO_4)_2$ for R^{3+} = Al, Sc и Fe and tungstate $KSc(WO_4)_2$, Kristallografiya 15 (5) (1970) 953-959 .

View Article Online
DOI: 10.1039/D1CE00118C

25. K. Okada and J. Ossaka, Structures of potassium sodium sulphate and tripotassium sodium disulphate, Acta Crystallog. B 36 (1980) 919-921.

26. A. Waskowska, L. Gerward, J. Staun Olsen, W. Morgenroth, M. Maczka, K. Hermanowicz, Temperature- and pressure-dependent lattice behaviour of $RbFe(MoO_4)_2$, J. Phys.: Condens. Matter 22 (2010) 055406.

27. X. Jiang, Y. Li, T. Li, Zh. Ning, Y. Zhao, M. Liu, Ch. Wang, X. Lai, J. Bi, D. Gao, Fabrication, microstructures, luminescent and magnetic properties of $LiFe(WO_4)_2$ microcrystals, J. Mater Sci: Mater Electron (2017) 28:5584–5591.

28. P.V. Klevtsov, R.F. Klevtsova, J. Struct. Chem. Polymorphism of double molybdates and tungstates of monovalent and trivalent metals with composition $M^+R^{3+}(EO_4)_2$ 18 (3) (1977) 339–355.

29. S.T. Bramwell, S.G. Carling, C.J. Harding, K.D.M. Harris, B.M. Kariuki, L. Nixon. I.P. Parkin, The anhydrous alums as model triangular-lattice magnets, J. Phys.: Condens. Matter 8 (9) (1996) L123–L129.

30. T. Inami, Y Ajiro, T Goto, Magnetization process of the triangular lattice antiferromagnets, $RbFe(MoO_4)_2$ and $CsFe(SO_4)_2$, J. Phys. Soc. Japan 65 (1996) 2374-2376.

31. H. Serano-Gonz´alez, S.T. Bramwell, K.D.M Harris, B.M. Kariuki, L. Nixon, I.P. Parkin, C. Ritter, Structural and magnetic characterization of the frustrated triangular-lattice antiferromagnets $CsFe(SO_4)_2$ and $RbFe(SO_4)_2$, Phys. Rev. B 59 (1999) 14451-14460.

32. M. Maczka, A. Pietraszko, G.D. Saraiva, A.G. Souza Filho, W. Paraguassu, V. Lemos, C.A. Perottoni, M.R. Gallas, P.T.C. Freire, P.E. Tomaszewski, F.E.A. Melo, J. Filho Mendes. J. Hanuza, High pressure effects on the structural and vibrational properties of antiferromagnetic $KFe(MoO_4)_2$, J. Phys.: Condens. Matter 17 (2005) 6285–6300.

33. M. Kenzelmann, G. Lawes, A.B. Harris, G. Gasparovic, C. Broholm, A.P. Ramirez, G.A. Jorge, M. Jaime, S. Park, Q. Huang, A.Ya. Shapiro, L.A. Demianets, Direct transition from a disordered to a multiferroic phase on a triangular lattice, Phys. Rev. Lett. 98 (2007) 267205.

34. M. Wierzbicka-Wieczorek, U. Kolitsch, E. Tillmanns, Crystal chemistry and topology of Rb–M^{III} molybdates (M = Fe, Sc, In) and triclinic $Rb_2MO_4O_{13}$: Novel building blocks, decorated chains and layers, Z. Kristallogr. 224 (2009) 151-162.

35. K.M. Khal'baeva, S.F. Solodovnikov, E.G. Khaikina, Yu.M. Kadyrova, Z.A. Solodovnikova, O.M. Basovich, Phase formation features in the systems M_2MoO_4-$Fe_2(MoO_4)_3$ (M = Rb, Cs) and crystal structures of new double polymolybdates $M_3FeMo_4O_{15}$, J. Solid State Chem. 183 (2010) 712-719.

36. T. Namsaraeva, B. Bazarov, D. Mikhailova, N. Kuratieva, A. Sarapulova, A. Senyshyn, H. Ehrenberg, Orthomolybdates in the Cs-$Fe^{II,III}$-Mo-O system: $Cs_4Fe(MoO_4)_3$, $Cs_2Fe_2(MoO_4)_3$ and $CsFe_5(MoO_4)_7$, Eur. J. Inorg. Chem. (2011) 2832-2841.

37. V.V. Atuchin, O.D. Chimitova, T.A. Gavrilova, M.S. Molokeev, Sung-Jin Kim, N.V. Surovtsev, B.G. Bazarov, Synthesis, structural and vibrational properties of microcrystalline $RbNd(MoO_4)_2$, J. Cryst. Growth 318 (2011) 683-686.

38. V.V. Atuchin, O.D. Chimitova, S.V. Adichtchev, B.G. Bazarov, T.A. Gavrilova, M.S. Molokeev, N.V. Surovtsev, Zh.G. Bazarova, Synthesis, structural and vibrational properties of microcrystalline β-$RbSm(MoO_4)_2$, Mater. Lett. 106 (2013) 26-29.

39. Apex Suite, Version 2014, Bruker AXS Inc., Madison, WI, USA, 2014.

40. M.C. Burla, R. Caliandro, M. Camalli, B. Carrozzini, G.L. Cascarano, L. De Caro, C. Giacovazzo, G. Polidori, R. Spagna, *SIR2004*: an improved tool for crystal structure determination and refinement, J. Appl. Cryst. 38 (2005) 381-388.

41. G.M. Sheldrick, SHELX97 Release 97-2, University of Göttingen, Germany, 1998.

View Article Online
DOI: 10.1039/D1CE00118C

42. T. Roisnel, J. Rodriguez-Carvajal, WinPLOTR: A Windows tool for powder diffraction pattern analysis, Mater. Sci. Forum 378−381 (2001) 118−123.

43. K.L. Parry, A.G. Shard, R.D. Short, R.G. White, J.D. Whittle, A. Wright, ARXPS characterisation of plasma polymerised surface chemical gradients. Surf. Interface Anal., 38(11) (2006) 1497-1504.

44. J.H. Scofield, Hartree-Slater subshell photoionization cross-sections at 1254 and 1487 eV, J. Electron Spectrosc. Relat. Phenom. 8 (1976) 129–137

45. S. Tanuma, C.J. Powell, D.R. Penn, Calculations of electron inelastic mean free paths. IX. Data for 41 elemental solids over the 50 eV to 30 keV range. Surf. Interface Anal., 43(3) (2011) 689-713.

46. S.J. Clark, M.D. Segall, C.J. Pickard, P.J. Hasnip, M.J. Probert, K. Refson, M.C. Payne, First pronciples methods using CASTEP, Z. Kristallog. 220 (2005) 567-570.

47. V. Milman, K. Refson, S.J. Clark, C.J. Pickard, J.R. Yates, S.-P. Gao, P.J. Hasnip, M.I.J. Probert, A. Perlov, M.D. Segall, Electron and vibrational spectroscopies using DFT, plane waves and pseudopotentials: CASTEP implementation, J. Mol. Struct: THEOCHEM 954 (1-3) (2010) 22-35.

48. M.C. Payne, M.P. Teter, D.C. Allan, T.A. Ariac, J.D. Joannopoulos, Iterative minimization techniques for ab initio total energy calculations – molecular dynamics and conjugate gradients, Rev. Modern Phys. 64 (4) (1992) 1045-1097.

49. D.M. Ceperley, B.J. Alder, Ground state of the electron gas by c stochastic method, Phys. Rev. Lett. 45 (7) (1980) 566-569.

50. J.P. Perdew, A. Zunger, Self-interaction correction to density-functional approximation for many-electron systems, Phys. Rev. B 23 (10) (1981) 5048-5079.

51. A.M. Rappe, K.M. Rabe, E. Kaxiras, J.D. Joannopoulos, Optimized pseudopotentials, Phys. Rev. B 41 (2) (1990) 1227-1230.

52. L. Kleinman, D.M. Bylander, Efficacious form for model pseudopotentials, Phys. Rev. Lett. 48 (20) (1982) 1425-1428.

53. A. Roldán, M. Boronat, A. Corma, F. Illas, Theoretical confirmation of the enhanced facility to increase oxygen vacancy concentration in TiO_2 by iron doping, J. Phys. Chem. C 114 (14) (2010) 6511-6517.

54. F.H. ElBatal, Y.M. Hamdy, S.Y. Marzouk, UV–visible and infrared absorption spectra of transition metals-doped lead phosphate glasses and the effect of gamma irradiation, J. Non-Cryst. Solids 355 (50-51) (2009) 2439-2447.

55. V.V. Atuchin, A.S. Aleksandrovsky, O.D. Chimitova, T.A. Gavrilova, A.S. Krylov, M.S. Molokeev, A.S. Oreshonkov, B.G. Bazarov, J.G. Bazarova, Synthesis and spectroscopic properties of monoclinic α-$Eu_2(MoO_4)_3$, J. Phys. Chem. C 118 (2014) 15404-15411.

56. A.A. Savina, V.V. Atuchin, S.F. Solodovnikov, Z.A. Solodovnikova, A.S. Krylov, E.A. Maximovsky, M.S. Molokeev, A.S. Oreshonkov, A.M. Pugachev, E.G. Khaikina, Synthesis, structural and spectroscopic properties of acentric triple molybdate $Cs_2NaBi(MoO_4)_3$, J. Solid State Chem. 225 (2015) 53-58.

57. B. G. Bazarov, A. E.Sarapulova, and Zh.G. Bazarova An IR and Raman Study of Trigonal Triple Molybdates $M^I_5M^{II}_{0.5}Hf_{1.5}(MoO_4)_6$($M^I$= K, Tl; M^{II}= Ca, Sr, Ba, Pb), Russian Journal of General Chemistry, 76(5) (2006) 677-681.

58. A. V. Gur'ev, G. Flor, A. Marini, V. Massarotti, and R. Riccardi, Characterization of the High Temperature Form of $Fe_2(MoO_4)_3$, Zeitschrift fur Naturforschung, 36(3) (1981) 280-282

59. A. E. Sarapulova, B. Bazarov, T. Namsaraeva, S. Dorzhieva, J. Bazarova, V. Grossman, A. A. Bush, I. Antonyshyn, M. Schmidt, A. M. T. Bell, M. Knapp, H. Ehrenberg, J. Eckert, and D. Mikhailova, Possible Piezoelectric Materials $CsMZr_{0.5}(MoO_4)_3$ (M = Al, Sc, V, Cr, Fe, Ga, In) and $CsCrTi_{0.5}(MoO_4)_3$: Structure and Physical Properties, J. Phys. Chem. C, 118 (2014) 1763−1773

View Article Online
DOI: 10.1039/D1CE00118C

60. J. G. Choi and L. T. Thompson, XPS study of as-prepared and reduced molybdenum oxides, Appl. Surf. Sci., 93 (1996) 143–149.

61. T. Herdt, M. Bruns, J. J. Schneider, A 3D MoO_x/carbon composite array as a binder-free anode in lithium-ion batteries, Dalton Trans., 42 (2018) 14897

62. K. Shimizu, A. Shchukarev, P. A. Kozin, J.-F. Boily, X-ray photoelectron spectroscopy of fast-frozen hematite colloids in aqueous solutions. 4. Coexistence of alkali metal (Na+,K+,Rb+,Cs+) and chloride ions, Surface Science, 606(13-14) (2012) 1005-1009.

63. A.V. Shchukarev, D.V. Korolkov, XPS study of Group IA carbonates, Cent. Europ. J. Chem., 2 (2) (2004) 347-362.

64. M. Wahlqvist, A. Shchukarev, XPS spectra and electronic structure of Group IA sulfates, J. Elect. Spectr. Rel. Phenom. 156-158 (2007) 310-314.

65. V.V. Atuchin, V.G. Kesler, Guangsi Meng, Z.S. Lin, The electronic structure of $RbTiOPO_4$ and the effects of the A-site cation substitution in $KTiOPO_4$-family crystals, J. Phys.: Condens. Matter. 24 (2012) 405503.

66. V.V. Atuchin, A.S. Aleksandrovsky, O.D. Chimitova, Cheng-Peng Diao, T.A. Gavrilova, V.G. Kesler, M.S. Molokeev, A.S. Krylov, B.G. Bazarov, J.G. Bazarova, Zheshuai Lin, Electronic structure of β-$RbSm(MoO_4)_2$ and chemical bonding in molybdates, Dalton Trans. 44 (2015) 1805-1815.

67. V.V. Atuchin, S.V. Adichtchev, B.G. Bazarov, Zh.G. Bazarova, T.A. Gavrilova, V.G. Grossman, V.G. Kesler, G.S. Meng, Z.S. Lin, N.V. Surovtsev, Electronic structure and vibrational properties of $KRbAl_2B_2O_7$, Mater. Res. Bull. 48 (2013) 929-934.

68. V.V. Atuchin, O.Y. Khyzhun, O.D. Chimitova, M.S. Molokeev, T.A. Gavrilova, B.G. Bazarov, J.G. Bazarova, Electronic structure of β-$RbNd(MoO_4)_2$, J. Phys. Chem. Solids, 77 (2015) 101-108.

69. A. P. Grosvenor, B. A. Kobe, M. C. Biesinger and N. S. Mcintyre, Investigation of multiplet splitting of Fe 2p XPS spectra and bonding in iron compounds, Surf. Interface Anal. 36 (2004) 1564 – 1574

70. M. C. Biesinger, B. P. Payne, A. P.Grosvenor, L. W. M. Lau, A. R. Gerson, R. St.C. Smart, Resolving surface chemical states in XPS analysis of first row transition metals, oxides and hydroxides: Cr, Mn, Fe, Co and Ni, Applied Surface Science, 257 (7) (2011) 2717-2730

71. D. J. Miller, M. C. Biesinger, N. S. McIntyre, Interactions of CO_2 and CO at fractional atmosphere pressures with iron and iron oxide surfaces: one possible mechanism for surface contamination?, Surf. Interface Anal. 33(4) (2002) 299-305

Table 1. Crystallographic data obtained for $RbFe_5(MoO_4)_7$

Empirical formula	$RbFe_5(MoO_4)_7$
Formula weight	1484.26 g/mol
Temperature	293(2) K
Wavelength	0.71073 Å
Crystal system	Monoclinic
Space group	$P2_1/m$ (11)
Unit cell dimensions	a = 6.8987(4) Å
	b = 21.2912(12) Å
	c = 8.6833(5) Å
	β=102.1896(18)°
Volume	V = 1246.66(12) Å^3
Z	2
Density (calculated)	3.9538 g/cm^3
Absorption coefficient	8.256
F(000)	1370
Crystal size	0.13 x 0.09 x 0.06 mm
Theta range for data collection	2.40– 32.93
Index ranges	-10 ≤ h ≤ 10, -32 ≤ k ≤ 32, -13 ≤ l ≤ 13
Reflections collected	93509
Independent reflections	4783 (R_{int} = 0.0342)
Completeness to theta = 32.93°	99.9 %
Refinement method	Full-matrix least-squares on F^2

Data / restraints / parameters	4783 / 0 / 193
Goodness-of-fit on F^2	1.067
Final R indices ($I>2\sigma_I$)	R_1 = 0.0166, wR_2 = 0.0334
Largest diff. peak and hole	3.171 and -2.134 e/Å $^{-3}$

Table 2. Factor group analysis of the unit cell vibrations for the monoclinic space group of $P2_1/m$

Free ion MoO_4^{2-}, T_d	Site symmetry C_s	Factor group symmetry ($Z = 2$) C_{2h}	Expected Raman bands	Observed Raman bands
$\nu_1(A_1)$ - $\nu_s(MoO_4)$	$A_1 \rightarrow A'$	$A' \rightarrow A_g+B_u$	A_g	926, 945
$\nu_2(E)$ - $\delta_s(MoO_4)$	$E \rightarrow A'+A''$	$A' \rightarrow A_g+B_u$ $A'' \rightarrow A_u+B_g$	A_g+B_g	249, 337
$\nu_3(F_2)$ - $\nu_{as}(MoO_4)$	$F_2 \rightarrow 2A'+A''$	$2(A_g+B_u)+ (A_u+B_g)$	$2A_g+B_g$	753, 805, 877
$\nu_4(F_2)$ - $\delta_{as}(MoO_4)$	$F_2 \rightarrow 2A'+A''$	$2(A_g+B_u)+ (A_u+B_g)$	$2A_g+B_g$	402

Captions

Figure 1. Three-dimensional framework structure of $RbFe_5(MoO_4)_7$. The (a) (001) and (b) (010) projections are shown. The unit cell is outlined. The FeO_6 octahedra and MoO_4 tetrahedra are shown by green and violet colors, respectively. Rb ions are the big yellow balls.

Figure 2. Raman spectrum of a $RbFe_5(MoO_4)_7$ single crystal.

Figure 3. Room-temperature X-ray diffraction pattern of $RbFe_5(MoO_4)_7$. Observed (red) and calculated (black) profiles, based on the Rietveld refinement of a structural model derived from the single crystal analysis, together with their difference curve (blue).

Figure 4. SEM images of obtained polycrystalline material at different magnifications.

Figure 5. (a) Temperature (ZFC- and FC mode) and (b) field dependencies of magnetization for polycrystalline $RbFe_5(MoO_4)_7$. (c) Temperature dependence of inverse susceptibility. Red line represents the modified Curie-Weiss fitting for susceptibility.

Figure 6. DSC results obtained from $RbFe_5(MoO_4)_7$ for the temperature range of 298-1073 K.

Figure 7. Temperature dependence and thermal expansion coefficients for the cell parameters of $RbFe_5(MoO_4)_7$, ppm=10^{-6}.

Figure 8. XPS spectra of the constituent element core levels of $RbFe_5(MoO_4)_7$.

Figure 9. Comparison of the experimental XPS spectrum and the calculated band structure of $RbFe_5(MoO_4)_7$.

View Article Online
DOI: 10.1039/D1CE00118C

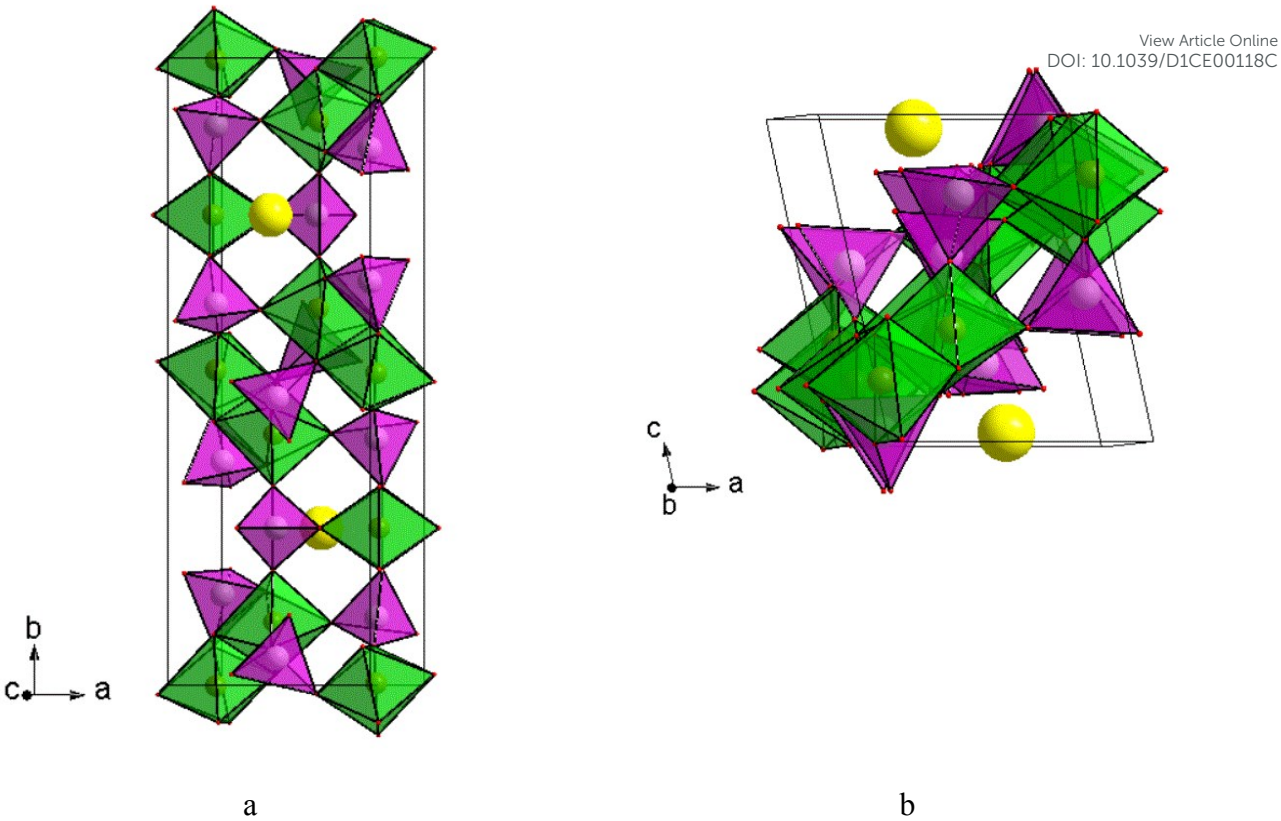

a b

Figure 1

View Article Online
DOI: 10.1039/D1CE00118C

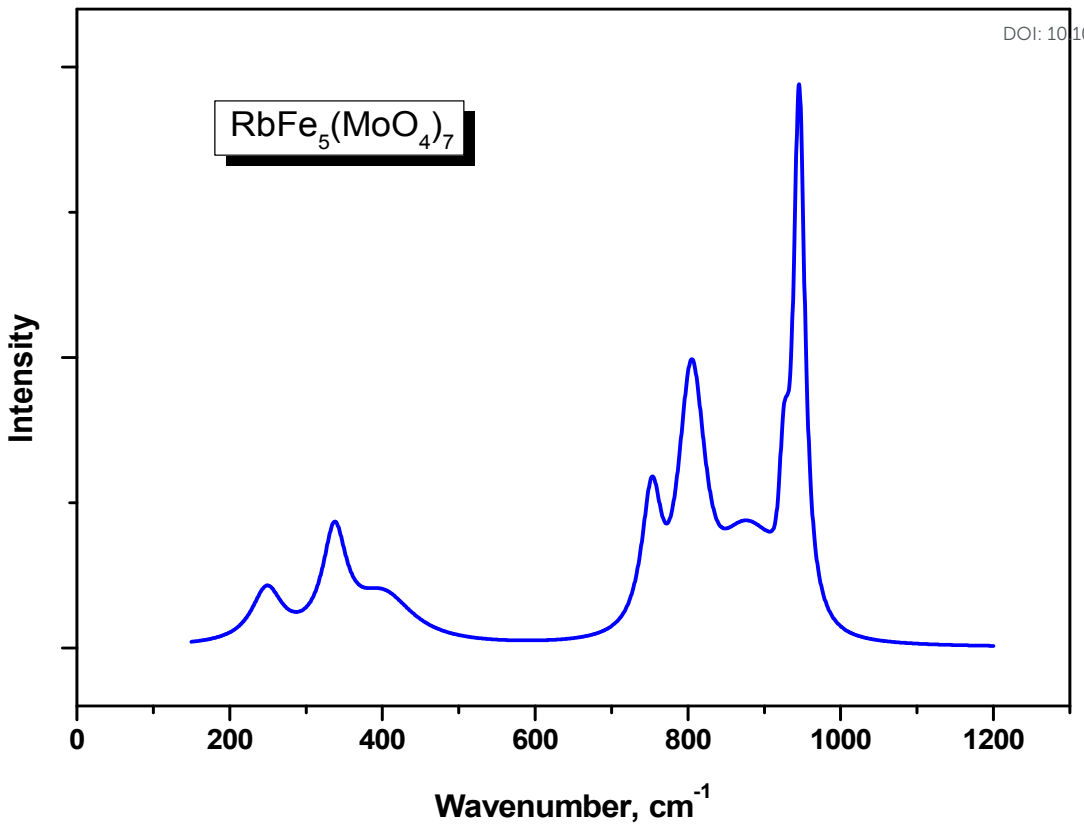

Figure 2

View Article Online
DOI: 10.1039/D1CE00118C

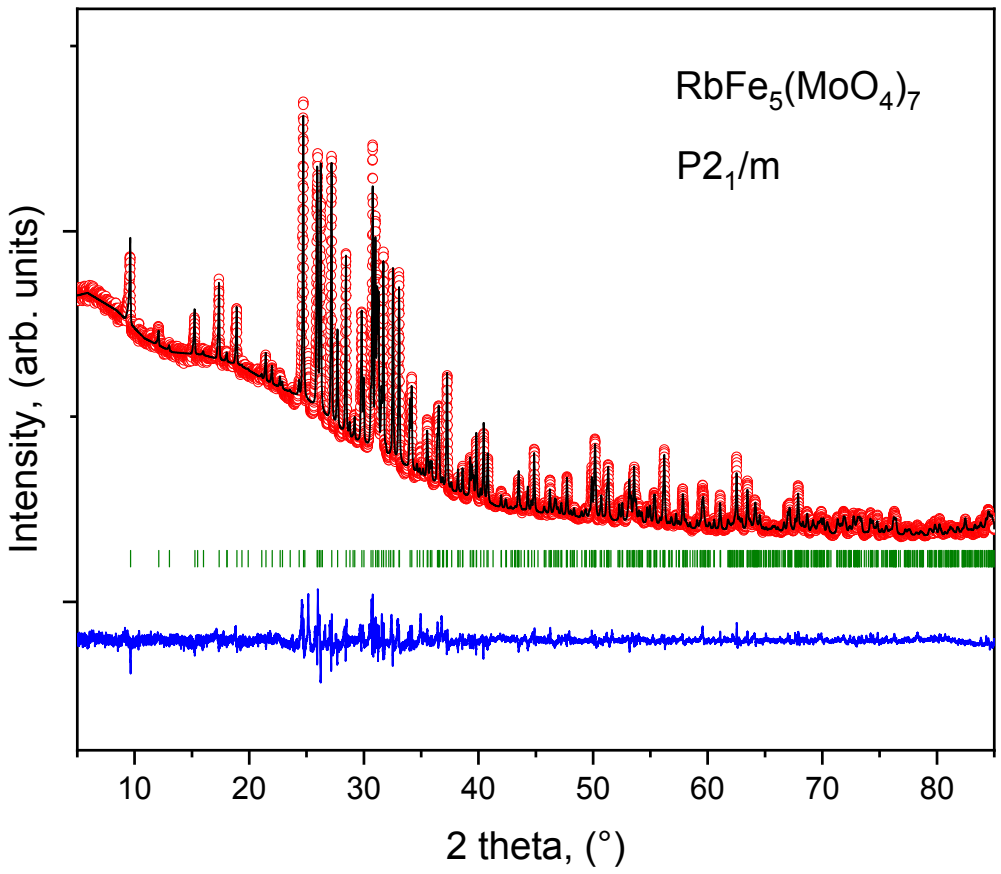

Figure 3

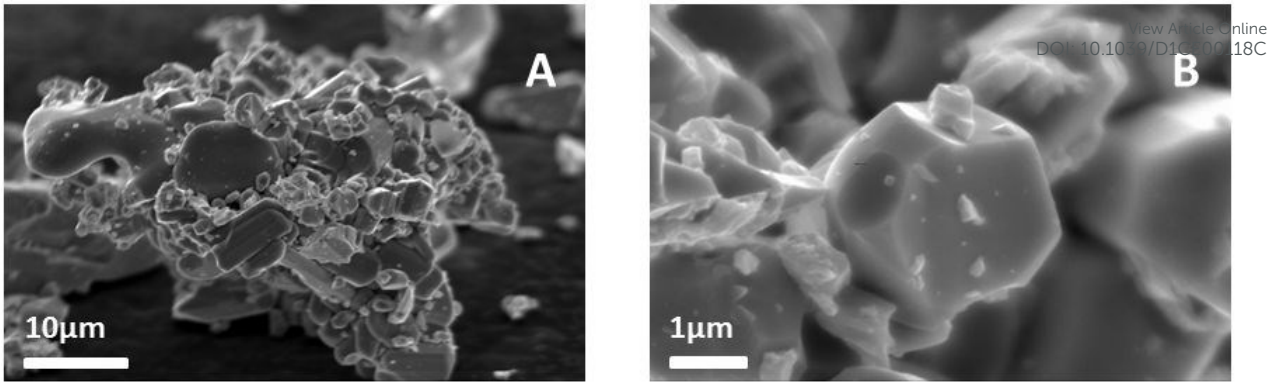

Figure 4

(a)

View Article Online
DOI: 10.1039/D1CE00118C

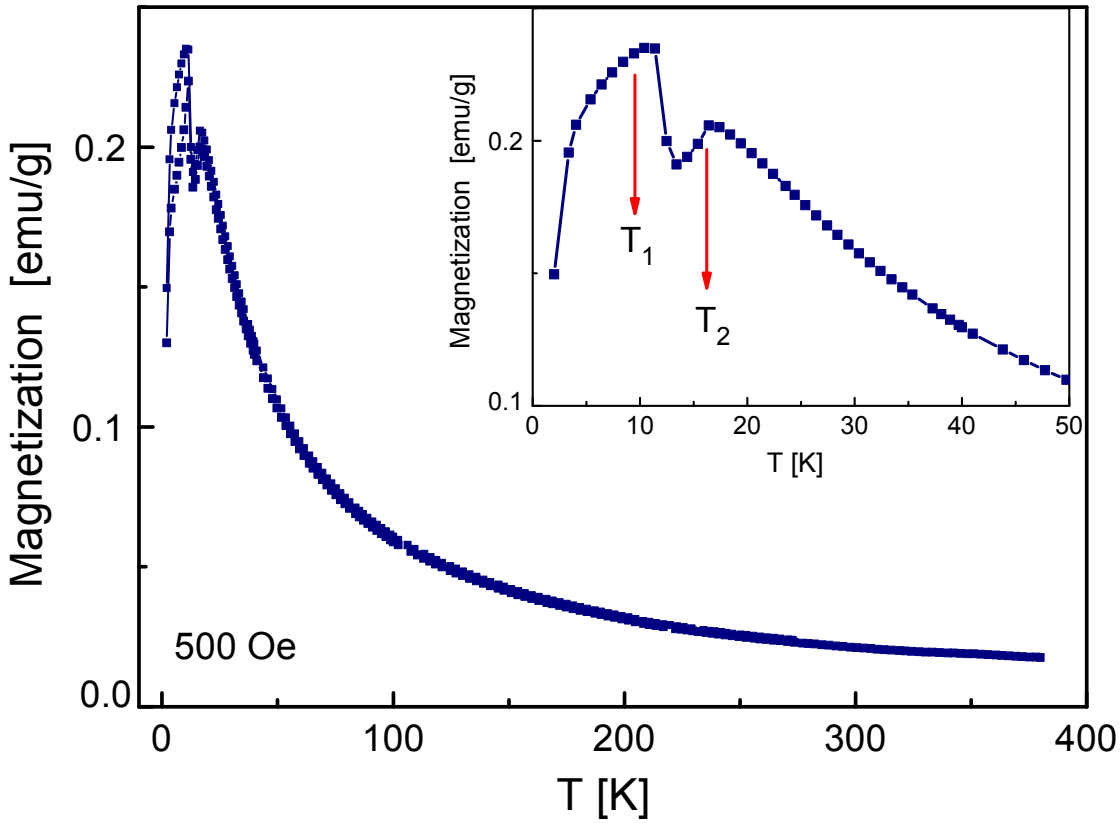

View Article Online
DOI: 10.1039/D1CE00118C

(b)

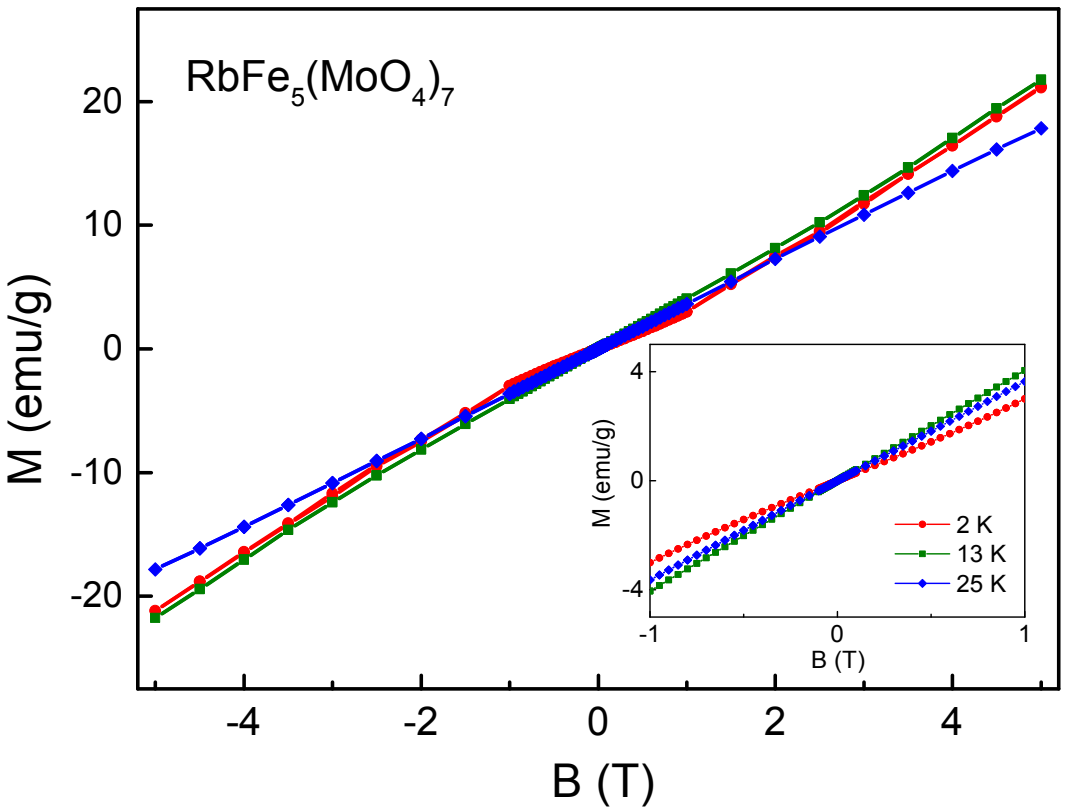

(c)

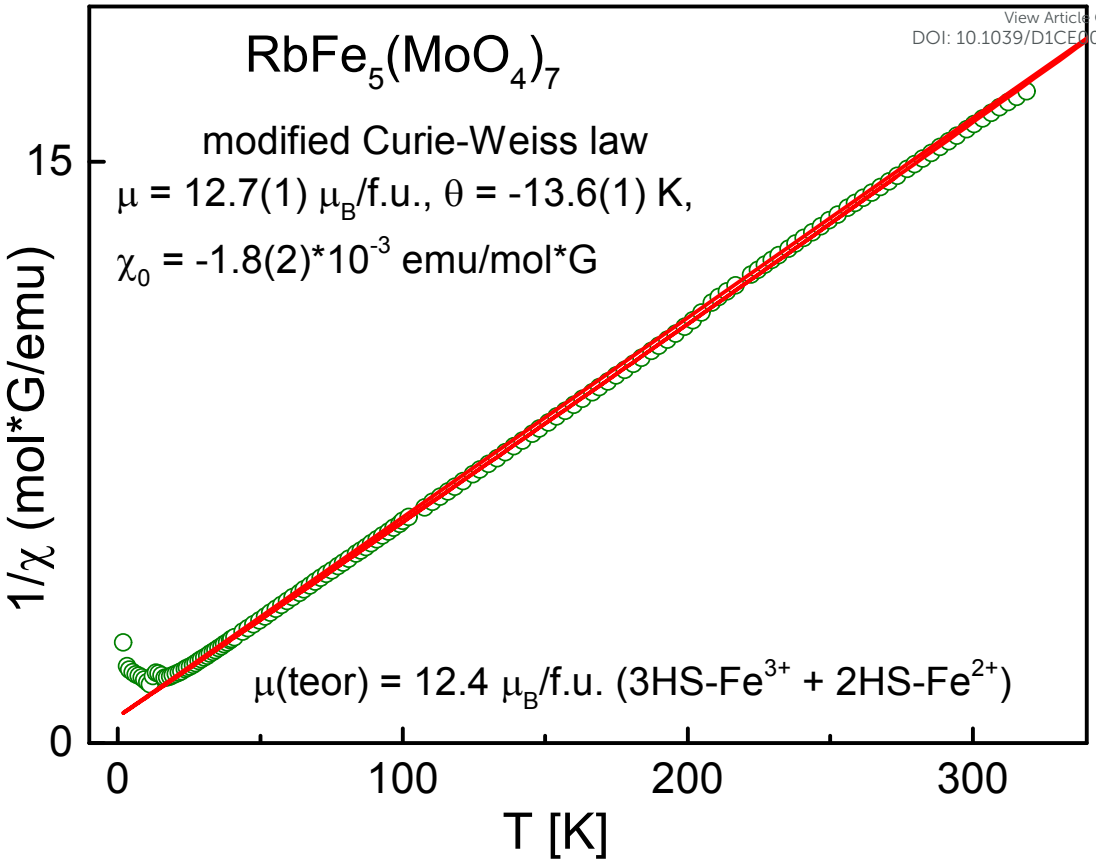

Figure 5

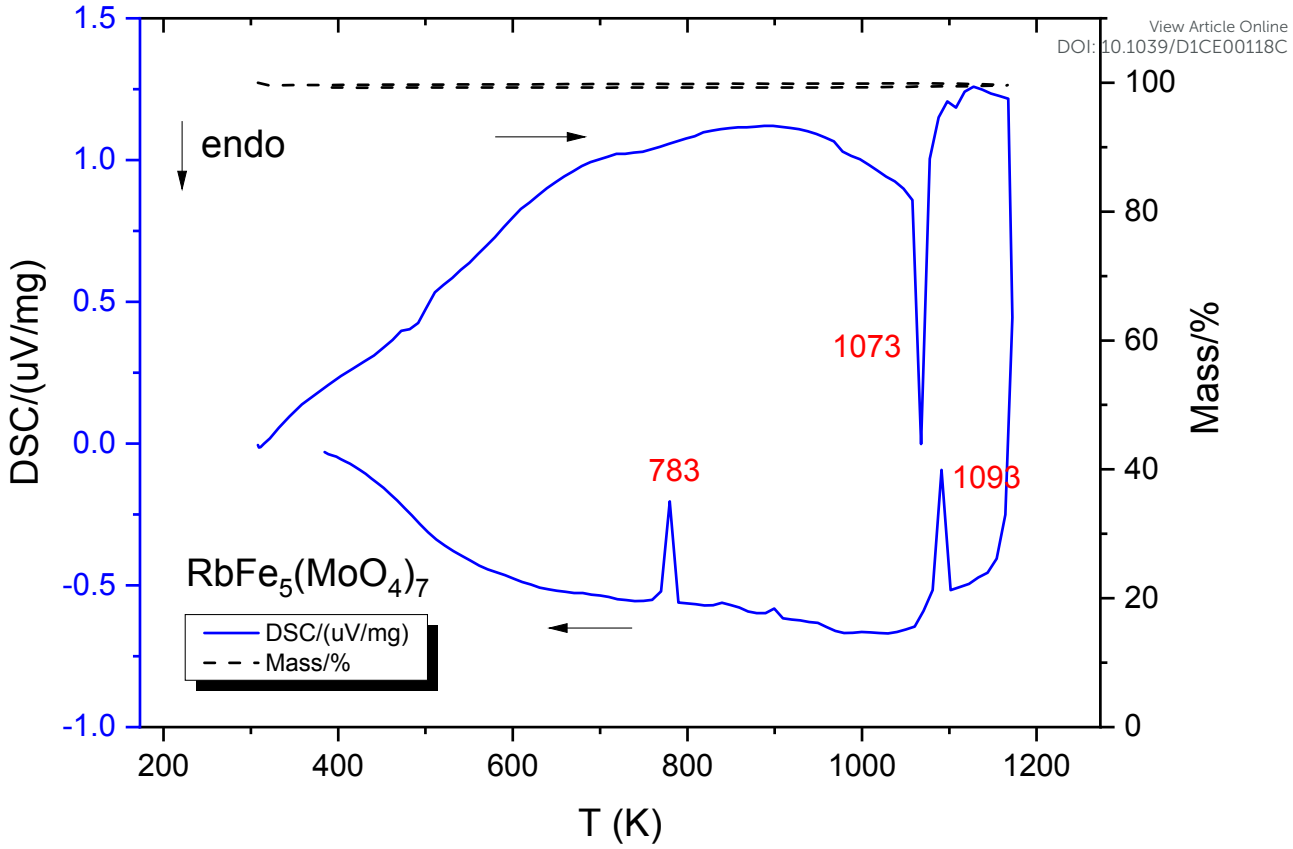

Figure 6

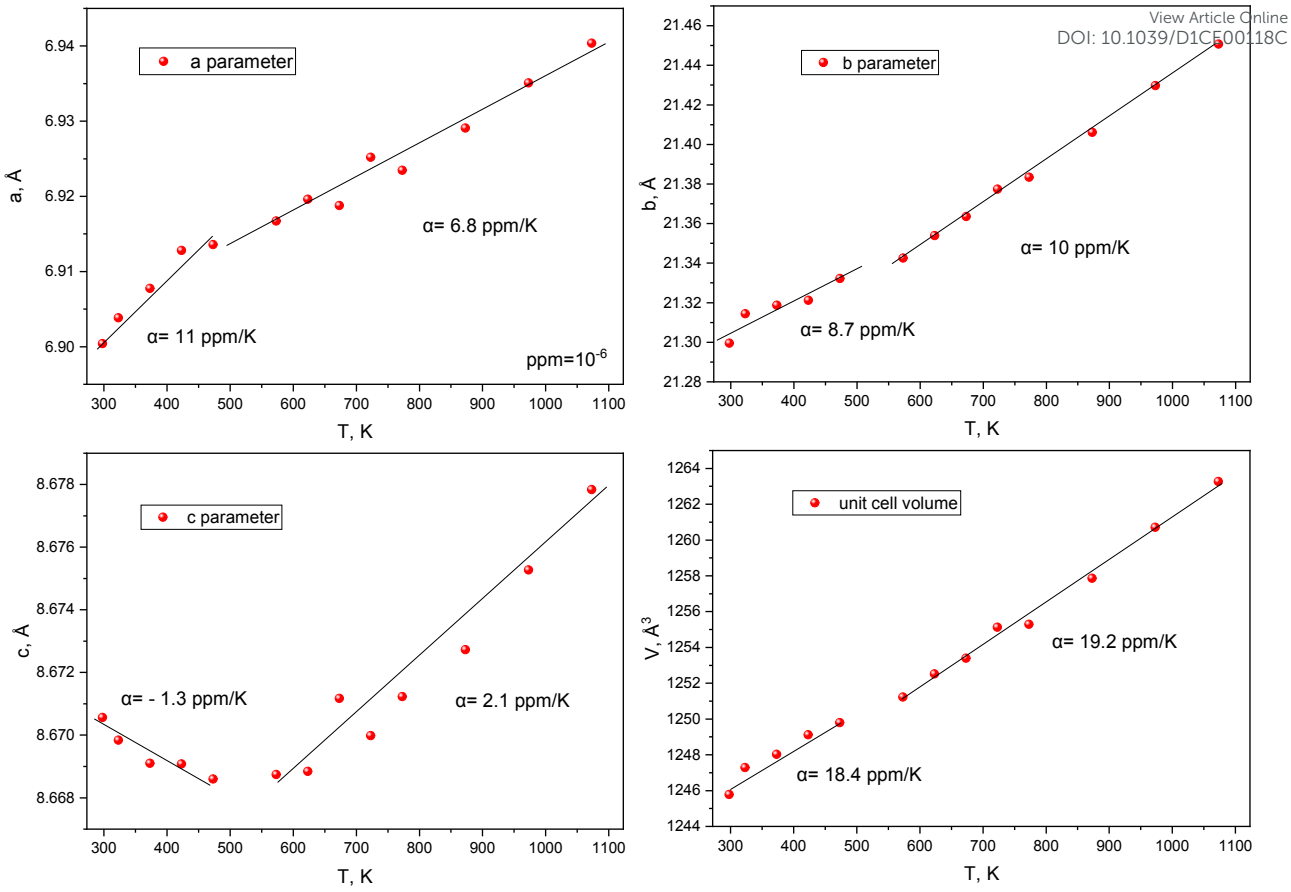

Figure 7

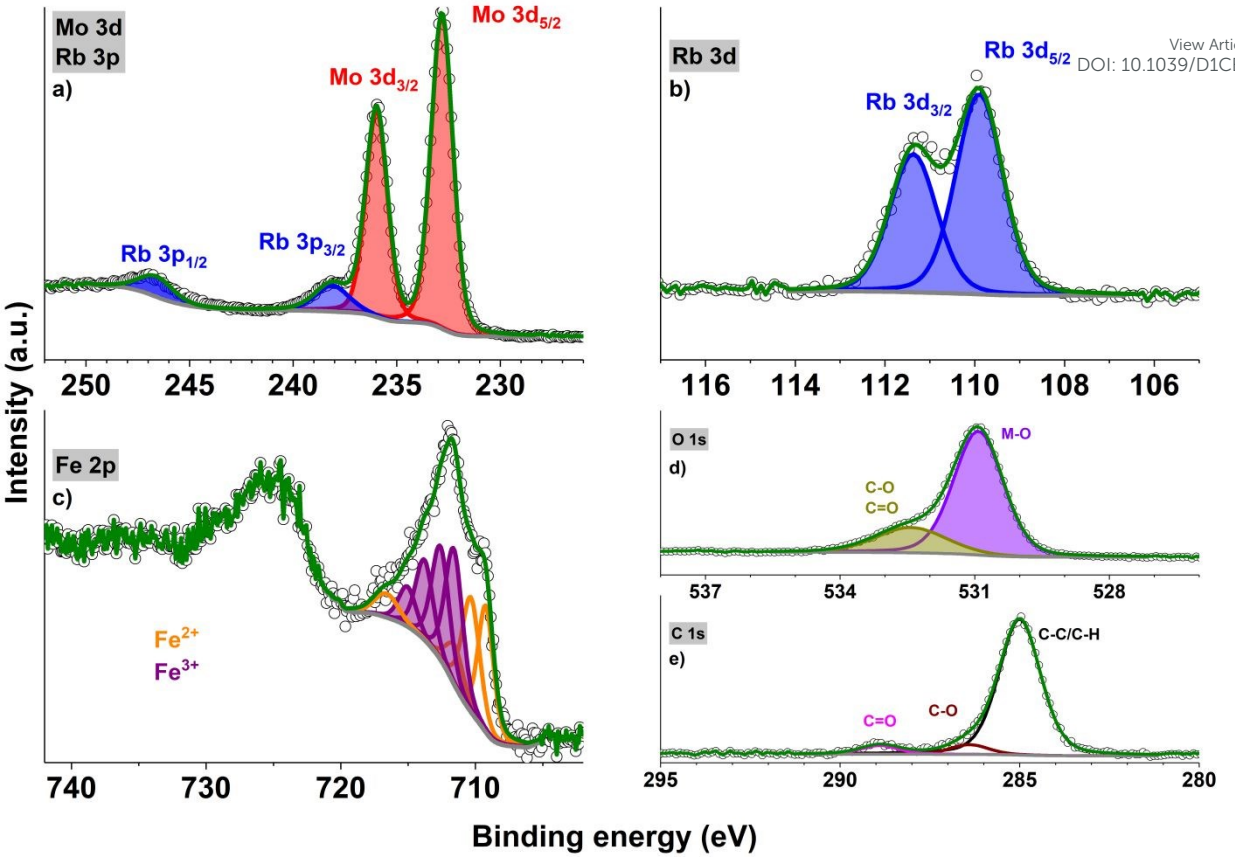

Fogure 8

View Article Online
DOI: 10.1039/D1CE00118C

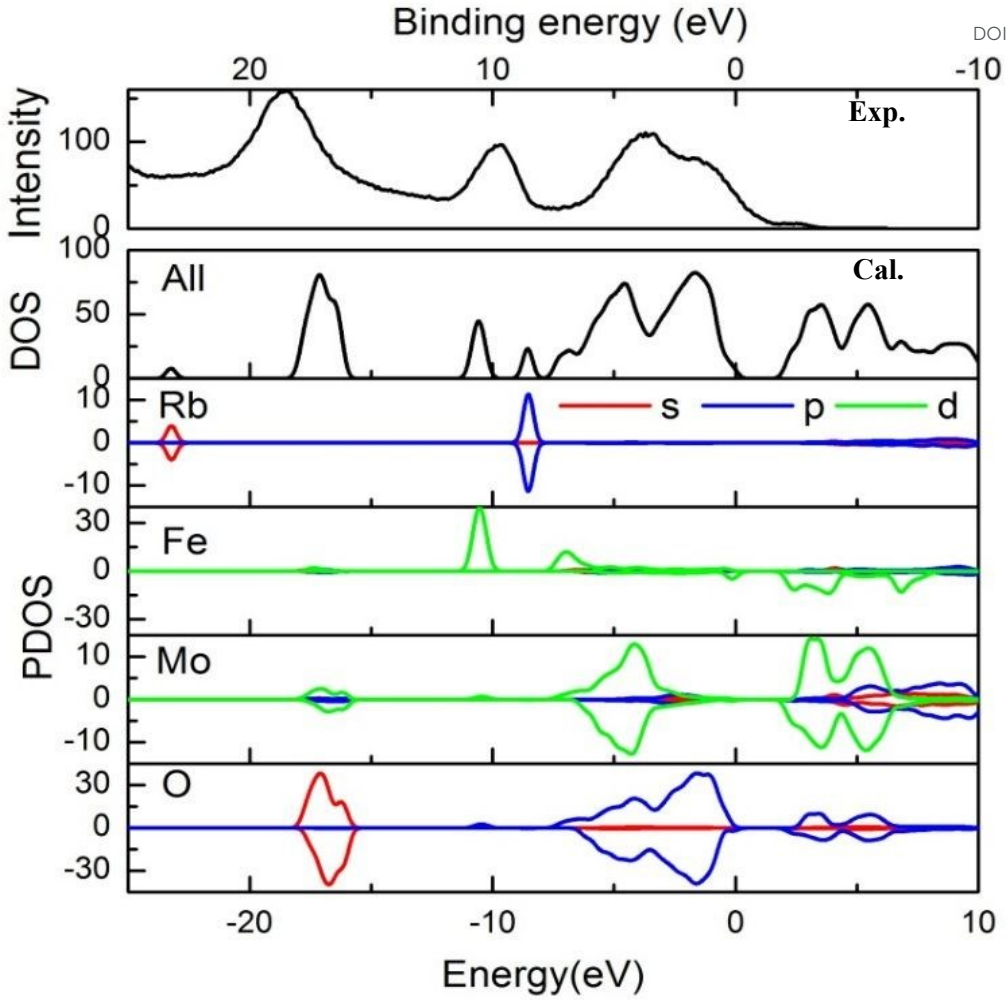

Figure 9